ELSEVIER

Assessment of a porous viscoelastic model for wave attenuation in ice-covered seas

Boyang Xu[1], Philippe Guyenne [*,1]

Department of Mathematical Sciences, University of Delaware, DE 19716, USA

ARTICLE INFO

ABSTRACT

Chen et al. (2019) recently proposed a two-dimensional continuum model for linear gravity waves propagating in ice-covered seas. It is based on a two-layer formulation where the ice cover is viewed as a porous viscoelastic medium. In the present paper, extensive tests against both laboratory experiments and field observations are performed to assess this model's ability at describing wave attenuation in various types of sea ice. The theoretical predictions are fitted to data on attenuation rate via error minimization and numerical solution of the corresponding dispersion relation. Detailed comparison with other existing viscoelastic theories is also presented. Estimates for effective rheological parameters such as shear modulus and kinematic viscosity are obtained from the fits and are found to vary significantly among the models. For this poroelastic system, the range of estimated values turns out to be relatively narrow in orders of magnitude over all the cases considered. Against field measurements from the Arctic Ocean, this model is able to reasonably reproduce the roll-over of attenuation rate as a function of frequency. Given the rather large number of physical parameters in such a formulation, a sensitivity analysis is also conducted to gauge the relevance of a representative set of them to the attenuation process.

1. Introduction

In recent decades, the polar regions have experienced major transformations due to global warming. For example, the rapid decline of summer ice extent in the Arctic Ocean has caught a lot of attention. While there is no doubt that warmer temperatures have been a major factor in transforming the polar seascape, evidence has also shown that ocean waves and their increased activity play an aggravating role, and in turn the presence of sea ice affects the wave dynamics. By breaking up the sea ice, waves cause it to become more fragmented, which in turn increases their capacity to further penetrate and damage the ice cover. A typical setting in the ocean where wave–ice interactions prevail is the marginal ice zone (MIZ) which is the fragmented part of the ice cover closest to the open ocean. It is a highly heterogeneous region comprising various types of sea ice that result from the incessant assault of incoming waves.

Of particular interest to oceanographers is the modeling of wave attenuation in sea ice, a process that has been poorly represented in large-scale wave forecasting models for the polar regions. There are two principal mechanisms for the attenuation of wave energy propagating into an ice field: (i) scattering by ice floes or other inhomogeneities of the ice cover, which is a conservative process that redistributes energy

in all directions, and (ii) dissipative processes which are related to various sources, e.g. friction due to the presence of sea ice, inelastic collisions and breakup of ice floes. The relative importance of scattering and dissipation is still unclear, and uncertainties still exist about the actual mechanisms for wave dissipation in sea ice. This has led to a surge of research activity on this topic in recent years. Studies have suggested that dissipative processes are dominant in frazil and pancake ice fields (Doble et al., 2015; Newyear and Martin, 1999), while scattering seems to be the main mechanism for wave attenuation in broken floe fields with appropriate floe size relative to the wavelength (Kohout and Meylan, 2008; Wadhams et al., 1988). Even for a denser ice field, the problem remains complex: e.g. Ardhuin et al. (2016) found that dissipation dominates over scattering for long swells in the Arctic ice pack.

With a view to describing wave attenuation in the MIZ, two different approaches have been pursued based on linear theory: (i) discrete-floe models where individual floes with possibly distinct characteristics are resolved assuming an idealized geometry (Bennetts and Squire, 2012; Kohout and Meylan, 2008; Montiel et al., 2016), and (ii) continuum models where the heterogeneous ice field is viewed as a uniform material with effective rheological properties including viscosity or

---

* Corresponding author.
E-mail addresses: boyangxu@udel.edu (B. Xu), guyenne@udel.edu (P. Guyenne).
[1] Both authors (B. Xu and P. Guyenne) contributed equally to the research and writing of this manuscript.

viscoelasticity (de Carolis and Desiderio, 2002; Keller, 1998; Wang and Shen, 2010b). In case (i), the analysis focuses on wave scattering and typically requires solving a boundary value problem with multiple regions in the horizontal hyperplane. By contrast, case (ii) enables the derivation of an exact algebraic expression for the dispersion relation governing traveling plane waves in the effective medium. Wave attenuation (possibly from scattering and dissipation combined) is encoded in the complex roots of this dispersion relation, and various physical effects are controlled by constant parameters. Recent reviews on this theoretical work can be found in Shen (2019) and Squire (2020).

Models of type (i) have been applied to various floe configurations and have reached a high degree of sophistication. There is now a consensus that the process of wave scattering in sea ice is well understood, and associated parameterizations have been tested for operational wave forecasting (Doble and Bidlot, 2013; Perrie and Hu, 1996; Williams et al., 2013a,b). It is however not the case for dissipative processes and, partly for this reason, there has been an increasing effort in recent years at developing and calibrating models of type (ii) (Cheng et al., 2017; de Santi et al., 2018; Doble et al., 2015; Rogers et al., 2016). In this framework, details of the attenuation processes are not accounted for and it lies on the calibration to ensure that the effective parameters are assigned suitable empirical values for practical applications.

While continuum models have been employed for some time now, based mostly on thin-plate theory, to describe wave propagation in pack ice (Fox and Squire, 1994; Liu and Mollo-Christensen, 1988), their extension to the setting of a more compliant or fragmented ice cover for application to the MIZ is more recent (Zhao et al., 2015). Earlier versions include the two-layer viscous model of Keller (1998) which treats the ice cover as a viscous layer lying on top of an ideal fluid (the ocean). The viscous layer is meant to represent a suspension of ice particles in water. Interaction among these particles and the associated friction leads to wave energy dissipation, which is modeled as a viscous effect. Good agreement has been found in comparison to laboratory data on wave attenuation in grease ice (Newyear and Martin, 1997, 1999). Keller's model was extended by de Carolis and Desiderio (2002) to allow for a viscous fluid in the lower layer as well. Validation was provided to some extent against laboratory and field measurements. Wang and Shen (2010b) refined Keller's model by adding elasticity to the upper layer as this property may be of relevance to broken floe fields. Their viscoelastic model has been tested against laboratory experiments under various ice conditions, and has been calibrated and used in parameterization of wave hindcasts for the Arctic and Antarctic. Building upon this idea, Zhao and Shen (2018) developed a three-layer version which features a turbulent boundary layer between the viscoelastic ice cover and the inviscid ocean. Dissipation due to turbulence in the middle layer is associated with some eddy viscosity.

In the spirit of this continuum approach, Chen et al. (2019) recently proposed a more elaborate two-layer model where the ice cover is viewed as a homogeneous isotropic poroelastic material according to Biot's theory (Chen et al., 2018). More specifically, the heterogeneous ice field is described as a mixed layer with a solid phase and a fluid phase as the two limiting configurations. Each phase is assumed to be slightly compressible. Dissipative effects are included via two different mechanisms: viscosity within each phase of the ice layer, and friction caused by the relative motion between its fluid and solid constituents. A parameter of interest in this model is the ice porosity which may serve to provide a measure of ice concentration. Despite the complicated nature of this formulation, an exact linear dispersion relation can be derived and numerical estimates of physically relevant solutions can be found using relatively simple selection criteria. Preliminary tests were conducted in Chen et al. (2019) to verify consistency with predictions from simpler models (e.g. open water, mass loading, purely elastic) in their respective limits (Collins et al., 2017; Xu and Guyenne, 2009). A more detailed review of this dispersion relation together with those from other viscoelastic representations will be presented in the next section.

The main goal of this paper is to further assess the porous viscoelastic model of Chen et al. (2019) by testing it against both laboratory experiments and field observations of wave attenuation in sea ice. These are taken from the literature, and allow us to probe a wide range of ice conditions and wave frequencies. This is accomplished by fitting the theoretical predictions to data on attenuation rate via error minimization over a set of rheological parameters. As a result, numerical estimates for both the attenuation rate and the set of effective parameters are obtained from the fitting process. This model's performance is also checked by comparing it to other existing viscoelastic formulations under the same various conditions. The purpose of such a comparison is two-fold. First, it helps examine in detail the parametric dependence in viscoelastic theories, and the extent to which common rheological parameters may differ in their range of values. Indeed, this difference may be of several orders of magnitude for such effective parameters. Second, it helps validate our data fitting method as we can check with previous independent calibration results from the literature. Given the relatively large parameter space in this poroelastic setting, a sensitivity analysis is also performed to gauge the individual contributions of rheological parameters to the fitting process. A notable finding from our study is that Chen et al.'s model can reproduce to some degree the roll-over of attenuation rate as observed in field measurements from the Arctic MIZ. This intriguing phenomenon has generally eluded linear scattering or viscoelastic models and, while various possible causes have been suggested, it is still not well understood (Li et al., 2017; Thomson et al., 2021).

The remainder of this paper is organized as follows. Section 2 recalls the linear dispersion relation obtained from the porous viscoelastic model of Chen et al. (2019) and describes the data fitting procedure. Other existing viscoelastic formulations are also briefly reviewed. Section 3 presents the corresponding fits to data on attenuation rate from a selection of laboratory experiments and field observations. Section 4 discusses the estimation of shear modulus and kinematic viscosity, and compares results among three different viscoelastic models. Section 5 shows sensitivity tests on a set of rheological parameters that are relevant to the poroelastic system. Finally, concluding remarks are provided in Section 6.

2. Theoretical models

The dispersion relations reviewed in this section are derived from continuum models for linear traveling waves in the two-dimensional case (one horizontal direction and one vertical direction).

The dispersion relation associated with the porous viscoelastic model proposed in Chen et al. (2019) (hereafter referred to as CGG) is given by

$$\omega^2 = \left(\frac{T_1 + g\,T_2}{T_3} \right) D_4 \tanh(D_4 H)\,, \qquad (1)$$

with

$$D_4 = \sqrt{\kappa^2 - \frac{\omega^2}{c_f^2}}\,,$$

where g is the acceleration due to gravity, H is the water depth and c_f is the speed of sound in water. The reader is directed to Chen et al. (2019) for a detailed derivation of this model and to the Appendix where the expressions of coefficients T_1, T_2, T_3 are recalled for convenience. These coefficients are functions of various wave parameters and rheological parameters. Wave parameters include the angular frequency ω and complex mode $\kappa = k + \mathrm{i}\,q$ where k is the wavenumber and q is the attenuation rate. Rheological parameters include the water density ρ_f as well as the ice density ρ_s, porosity β, shear modulus μ, Poisson's ratio ν, kinematic viscosity η and thickness h. Ice porosity is represented by a dimensionless parameter whose range is $0 \le \beta \le 1$, with the limiting values $\beta = 0$ (solid phase) and $\beta = 1$ (fluid phase) corresponding to pack ice and near-open water,

respectively. This parameter may be related to ice concentration C via the relation $\beta = 1 - C$, namely β is the complement of C. It should be pointed out that, in this continuum framework, the elasticity, porosity and viscosity parameters do not necessarily correspond to intrinsic properties of sea ice but rather they are meant to represent effective properties of the heterogeneous ice field under consideration, similar to e.g. homogenization modeling of wave propagation in complex media (Craig et al., 2009; de Bouard et al., 2008). These parameters may thus vary over a wider range than the typical values for sea ice. In view are potential applications to large-scale wave forecasting in the MIZ where various types of sea ice coexist. Whenever the information is available, β and h will be assigned values corresponding to mean ice concentration and mean thickness of the ice cover (e.g. field studies often report an estimate of the fraction of ice-covered surface that may be used for C). Aside from bulk viscosity which is typically regulated by η, this model also describes friction due to the relative motion between fluid and solid parts of the ice field. In the equations, the coefficient controlling this mechanism is defined by

$$b = \frac{8\rho_s \eta \beta}{a^2}, \qquad (2)$$

where a denotes the fluid pore size in the porous medium. From the viewpoint of effective medium theory for wave propagation in the MIZ, this parameter a may be related to some characteristic horizontal size of open-water areas in the fragmented ice cover.

In the next section, predictions from (1) will be tested against a selection of laboratory experiments and field observations. For each set of experimental data, comparison with other existing models will be provided as well. These include recent viscoelastic models by Wang and Shen (2010b) and Mosig et al. (2015), which we find convenient to present in detail below because they share common rheological parameters, and this will be of relevance to the subsequent discussion. These two models are simpler than the present one in the sense that they do not take into account ice porosity, accordingly their dispersion relations are simpler. The dispersion relation resulting from Wang and Shen's model (Wang and Shen, 2010b) (hereafter referred to as WS) can be written as

$$\omega^2 = \left(1 + \frac{\rho_s N_3}{\rho_f N_4}\right) g\kappa \tanh(\kappa H), \qquad (3)$$

where

$$
\begin{aligned}
N_4 =\ & g\kappa \left[4\kappa^3 N_1 \eta_c^2 \sinh(\kappa h) \cosh(N_1 h) + N_2^2 \cosh(\kappa h) \cosh(N_1 h) \right. \\
& \left. - g\kappa \sinh(\kappa h) \sinh(N_1 h)\right], \\
N_3 =\ & (g^2\kappa^2 - N_2^4 - 16\kappa^6 N_1^2 \eta_c^4) \sinh(\kappa h) \sinh(N_1 h) \\
& - 8\kappa^3 N_1 \eta_c^2 N_2^2 \left[\cosh(\kappa h) \cosh(N_1 h) - 1\right],
\end{aligned}
$$

and

$$N_2 = \omega + 2\mathrm{i}\,\eta_c \kappa^2, \quad N_1 = \sqrt{\kappa^2 - \mathrm{i}\frac{\omega}{\eta_c}}, \quad \eta_c = \eta + \mathrm{i}\frac{\mu}{\rho_s \omega}.$$

On the other hand, the dispersion relation produced by Mosig et al.'s model (Mosig et al., 2015) (hereafter referred to as EFS) takes the form

$$\frac{\omega^2}{g - \frac{\rho_s \omega^2 h}{\rho_f} + \frac{\mu_c h^3 \kappa^4}{6(1-\nu)\rho_f}} = \kappa \tanh(\kappa H), \qquad (4)$$

where

$$\mu_c = -\mathrm{i}\,\rho_s \omega \eta_c = \mu - \mathrm{i}\,\omega \rho_s \eta. \qquad (5)$$

Note that the EFS model also makes use of the thin-plate approximation and thus is significantly simpler than both CGG and WS models which instead consider the ice cover as a distinct layer with an actual thickness. Preliminary comparison between these three models can be found in Chen et al. (2019).

For a given value of ω and other parameter values, the dispersion relation is solved numerically for κ using the root-finding routine *fsolve* in Matlab. More specifically, because κ is complex, Eq. (1) is split up into its real and imaginary parts. This leads to a system of two independent equations that are solved simultaneously for the two unknowns k and q. The *fsolve* algorithm is essentially a quasi-Newton method with a numerical approximation of the Jacobian matrix. We have successfully used this Matlab routine in previous work (Guyenne, 2006; Guyenne and Părău, 2014) to compute traveling wave solutions of nonlinear partial differential equations. Considering that multiple roots for k and q may exist here (Mosig et al., 2015; Zhao et al., 2017), we apply the selection criteria proposed in Wang and Shen (2010b) to find a dominant pair (k, q) associated with a physically relevant solution. We choose the converged values $(k, q) \in \mathbb{R}_+^2$ such that k is closest to the open-water wavenumber k_0 which solves

$$\omega^2 = gk \tanh(kH),$$

and q is the lowest attenuation rate possible. Accordingly, we run the root finder *fsolve* for a range of initial guesses around $(k, q) = (k_0, 0)$ and select the converged values for which the error $|\kappa - (k_0 + \mathrm{i}\,0)|$ is minimum among all the roots found. In doing so, we were able to get acceptable solutions in all the cases we considered, via the data-fitting procedure as described below.

For the following tests, we prescribe a number of physical parameters such as $g = 9.81$, $\rho_s = 917$, $\rho_f = 1025$ and $c_f = 1449$ (in SI units), and fit the model predictions to the experimental data by optimizing with respect to other parameters. The water depth H is also specified, since this is either known information from laboratory experiments or a representative value may be used for a specific oceanic region when comparing to field observations. Furthermore, because the range of Poisson's ratio is typically small ($0 < \nu < 1/2$), we set it to be $\nu = 0.4$, after checking that it does indeed not play a major role (see Section 5). This reduction in the parameter space helps simplify the analysis, which is especially relevant for the CGG model considering that it involves many physical parameters.

We will focus our attention on the subset (β, μ, η) when fitting the model predictions to the experimental data. These three parameters are representative of porous viscoelastic properties of the ice cover, and two of them (μ and η) are common to the CGG, EFS and WS models. We will give a detailed comparison of (μ, η) estimated from these three models in Section 4. Throughout this study, we will only consider data on the attenuation rate, a reason being that data on the wavenumber were not reported by field observations and our focus here is on the attenuation process as in Kohout and Meylan (2008), Mosig et al. (2015), Perrie and Hu (1996) and Sutherland et al. (2019). Our fitting procedure is basically a direct search approach. For a given triplet (β, μ, η) and a range of values of ω, we apply the above-mentioned root-finding scheme to find a set of pairs (k, q). We repeatedly run this procedure over a specified region of parameter space (β, μ, η), and select the set $\{q_j\}$ for which the L^2 error

$$E = \sum_{j=1}^{n} (q_j - \hat{q}_j)^2, \qquad (6)$$

between numerical estimates $\{q_j\}$ and experimental data $\{\hat{q}_j\}$, is minimum among all the solutions calculated. The best fit so obtained returns a set $\{q_j\}$ for the attenuation rate, as well as a triplet (β, μ, η) for these rheological parameters. For the problem at hand, we use a straightforward definition (6) of the error as in de Santi et al. (2018), which is readily applicable to all the cases explored and which allows for a direct comparison among the various models involved.

It turns out that information on ice concentration was also reported in some of these studies (which we used to determine the ice porosity), and thus only the pair of parameters (μ, η) is to be found from the data fitting. In this process, the ranges of values for (μ, η) and their resolutions are chosen in a heuristic manner based on extensive trials, considering previous work (Mosig et al., 2015; Newyear and Martin, 1999; Zhao and Shen, 2015) and our own experience (Chen et al., 2019, 2018). The larger the region of parameter space to be covered, the higher the computational cost. Typically, we conduct a preliminary search over an extended rough region of parameter space and then refine the search over smaller better-resolved sectors. Aside from testing the performance of the CGG model, such an analysis also helps calibrate it by estimating rheological parameters for potential applications in realistic conditions. As discussed below, while the CGG, EFS and WS models share common physical parameters such as μ and η, their respective numerical values according to the data fitting may differ significantly. Note that we use the same procedure to obtain fitting curves from the EFS and WS models.

Although it is somewhat different in character from the CGG, EFS and WS models, we will also include a comparison with the two-layer viscous model recently proposed by Sutherland et al. (2019) (hereafter referred to as SRCJ), which estimates wave attenuation in sea ice by

$$q = \frac{1}{2}\Delta_0 \epsilon h k_0^2. \tag{7}$$

This formula is partly heuristic because it was derived based on scaling arguments and dimensional analysis. It is nonetheless appealing due to its stunning simplicity and has been shown to produce satisfactory results in comparison with experimental data. Considering that viscous models have been successful at describing wave attenuation in such ice covers as grease ice, predictions from (7) may serve as a suitable independent reference, especially for the tests involving laboratory experiments. The coefficients Δ_0 and ϵ are dimensionless empirical parameters whose range is $0 < \Delta_0 < 1$, $0 < \epsilon < 1$. The same L^2 error (6) is used to optimize (7) with respect to the pair (Δ_0, ϵ) when fitting to measurements. The parameter Δ_0 is a measure of the relative motion between ice and water at the bottom boundary of the ice layer. To first approximation, $\Delta_0 \simeq 1$ corresponding to a no-slip boundary condition. The parameter ϵ is thought to be a function of ice porosity, exhibiting a similar behavior. In particular, the limit $\epsilon \to 0$ is analogous to $\beta \to 0$ (pack ice) for which, according to (7), there should be no wave dissipation within the ice layer. Sutherland et al. (2019) pointed out that such a parameterization is consistent with observations of wave attenuation through the MIZ, being several orders of magnitude greater in frazil and pancake ice than in a broken floe field (Doble et al., 2015). This is somewhat counterintuitive considering that the latter represents a more rigid ice cover than the former. Note however that the dominant mechanism for wave attenuation in broken floe fields is believed to be scattering and is of different nature from the viscous-type dissipation taking place in pancake ice fields. Preliminary tests of the CGG model in Chen et al. (2019) are also consistent with these observations and indicate a tendency for q to decrease as $\beta \to 0$ over all frequencies.

As in Chen et al. (2019), for computational purposes, we non-dimensionalize the equations involved in the root-finding and data-fitting processes for each of these models. A motivation for this non-dimensionalization is to accommodate the large disparity in orders of magnitude among the various quantities at play in this problem. We typically use H, $\sqrt{H/g}$ and $\rho_f H^3$ as a characteristic length, time and mass respectively, to rescale the variables and parameters. We have examined different scaling choices (involving different multiples of the above characteristic values) and obtained similar results. For the discussion in the next sections, our numerical results are converted back to dimensional values.

3. Comparison with experimental data

In this section, we test the CGG model against three different sets of laboratory experiments and two different sets of field observations. Altogether, these span a wide range of wave frequencies and ice-cover types. In each case, the CGG model is tested by best fitting its predictions to experimental data on the attenuation rate, based on the numerical scheme described earlier. Predictions by other existing models are also shown for comparison and numerical values of their rheological parameters as determined by the data fitting are discussed.

3.1. Laboratory experiments of Newyear and Martin (1997)

Newyear and Martin (1997) conducted laboratory experiments of wave propagation and attenuation in grease ice. This study was among the first to measure wave attenuation by floating ice in a controlled laboratory environment. The wave tank was a flat-bottomed rectangular box, 3.5 m long, 1 m wide and 1 m deep. They reported two sets of measurements for two different ice thicknesses $h = 11.3$ cm (Test 1) and $h = 14.6$ cm (Test 2). In both cases, the water depth was set to $H = 0.5$ m and the ice concentration was estimated to be $C = 0.53$.

Fig. 1 shows best fits of the CGG, EFS and WS models to Newyear and Martin's measurements of attenuation rate q (from their Tables 1 and 2) as functions of wave frequency $f = \omega/(2\pi)$. The value $\beta = 1 - C = 0.47$ for ice porosity is used in the CGG model. Newyear and Martin (1999) provided a comparison of their laboratory data with Keller's two-layer viscous model (Keller, 1998), whose predictions are also shown in Fig. 1 (these were extracted from figures in their paper). Keller's model is basically a counterpart of WS model without elasticity. The agreement between the CGG model and the experiments is fairly good in both cases. We see that the CGG and EFS curves are particularly close together. They appear to be concave while Keller's curve appears to be convex, which is characteristic of a purely viscous (i.e. diffusive-type) mechanism (Liu et al., 1991; Sutherland et al., 2019). The CGG concavity is especially pronounced for $h = 14.6$ cm (Fig. 1b), which leads to a close fit at high frequencies where the increase of q seems to slow down. As for the WS curve, it behaves more linearly with respect to f and lies between these two opposite trends. Note that it is not clear whether the actual trend is concave or convex due to measurement errors and the limited number of data points.

3.2. Laboratory experiments of Wang and Shen (2010)

This study was conducted as part of the RECARO (REduced ice Cover in the ARctic Ocean) project in the Arctic Environmental Test Basin at Hamburg Ship Model Basin (HSVA), Germany. The wave basin was roughly 19 m long, 6 m wide and 1.5 deep, and was separated equally lengthwise into two 3 m wide flumes (referred to as Tank 2 and Tank 3). Experiments were performed in these two flumes to measure wave propagation and attenuation in a grease-pancake ice mixture (Wang and Shen, 2010a). The ice thickness was not uniform in these experiments, so we use the mean values $h = 9.0$ cm and 8.9 cm for Tank 2 and 3 respectively. The water depth was $H = 0.85$ m but no information was provided on the ice concentration.

Comparison of these experimental data (from Tables 1 and 2 in Wang and Shen, 2010a) with the CGG, EFS, SRCJ and WS predictions is given in Fig. 2. The general trend appears to be convex for most of these models. The EFS fit falls down very quickly as $f \to 0$ but seems to develop an inflection (from convex to concave) while rising up at high frequencies. The CGG fit looks satisfactory overall. It does not quite capture the high convexity around $f = 0.9$ Hz (in particular for Tank 3) but it does not fall down as quickly as the other curves at lower frequencies, which is consistent with the asymptotic behavior suggested by the experimental results in that limit. A similar observation was made by Wang and Shen (2010a) who found that a grease-pancake ice layer appears to be more dissipative (producing a higher attenuation
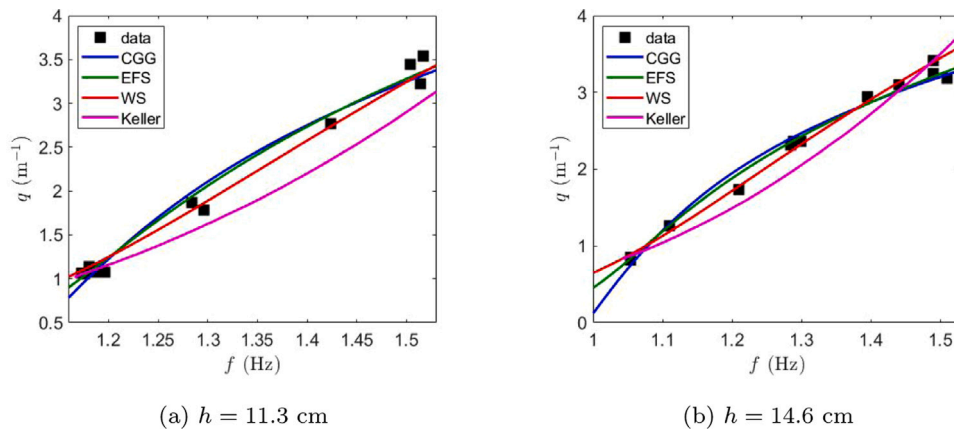
Fig. 1. Comparison of attenuation rate vs. frequency between model predictions and laboratory data for grease ice from Newyear and Martin (1997). Predictions from the CGG, EFS, WS and Keller's models are shown. Laboratory data for (a) $h = 11.3$ cm (test 1), (b) $h = 14.6$ cm (test 2) are presented.
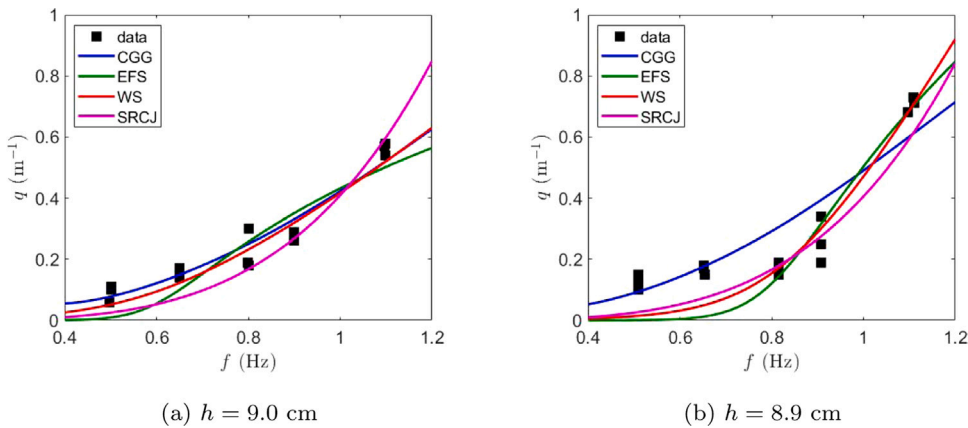

Fig. 2. Comparison of attenuation rate vs. frequency between model predictions and laboratory data for a grease-pancake ice mixture from Wang and Shen (2010a). Predictions from the CGG, EFS, SRCJ and WS models are shown. Laboratory data for (a) $h = 9.0$ cm (tank 2), (b) $h = 8.9$ cm (tank 3) are presented.

rate) in the low-frequency range than predicted by Keller's viscous model, and concluded that such a mixed ice layer may be rheologically quite different from a pure grease ice layer (for which a viscous model usually works well).

The CGG fit estimates the ice porosity to be $\beta = 0.16$ and 0.15 for Tank 2 and 3 respectively. These low values of β mimic a configuration where the ice cover is relatively compact, which is compatible with the presence of pancake ice, and as expected they are lower than the value $\beta = 0.47$ deduced from Newyear and Martin's measurements for grease ice. The associated pore sizes are given by $a = 1.2$ cm and 2.4 cm for Tank 2 and 3. Recall that the pores represent the fluid part of the porous ice cover in the continuum formulation of the CGG model. For low β, we may thus assume that constitutive elements of the solid part would have a typical size on the same order of magnitude as or larger than a, which is consistent with the pancake diameter ranging from about $\ell = 1$ cm to 40 cm as observed in Wang and Shen's experiments.

3.3. Laboratory experiments of Zhao and Shen (2015)

Zhao and Shen (2015) followed up with additional experiments at the HSVA in 2013. Three sets of measurements were performed in Tank 3 (as defined in the previous section) for three different types of ice cover: a frazil/pancake ice mixture (with thickness $h = 2.5$ cm), pancake ice ($h = 4.0$ cm) and a broken floe field ($h = 7.0$ cm). These three cases are referred to as Test 1, 2 and 3 respectively. The

water depth was about $H = 0.94$ m and again, although values for the diameter of a typical pancake/floe were reported in Zhao and Shen (2015), no information was given on the mean ice concentration for the generated ice fields.

Overall, the models compare well with these experiments (from Table 3 in Zhao and Shen, 2015), as indicated in Fig. 3. Their fits are especially good for Tests 1 and 2, and are reminiscent of the previous results (Fig. 2) with Wang and Shen's experiments for a grease-pancake ice mixture. The SRCJ model is found to perform quite well over the entire range of frequencies considered, even at low frequencies where, despite tending to zero, its fitting curve is closest to the data points. This contrasts with a previous observation regarding the comparison to Wang and Shen's experiments, and may be explained by the fact that the ice thicknesses for Tests 1 and 2 are significantly smaller than those specified in Wang and Shen (2010a). The agreement is less convincing for Test 3, partly because there are fewer data points available. These suggest a convex dependence of q on f, which is captured to some extent by the CGG, SRCJ and WS models. The laboratory measurements however yield much higher attenuation rates at low frequencies than what these models predict, indicating a tendency for q to saturate or even increase back as f decreases. The EFS curve looks quite different from the other curves, exhibiting a slightly concave profile. It is worth pointing out that all these models underestimate the attenuation rate at low frequencies for all three experiments.

From the CGG fit, we find $\beta = 0.01$, 0.07 and 0.06 for Test 1, 2 and 3 respectively. The corresponding pore sizes are $a = 2.0$ cm, 4.8 cm and

8.5 cm. Note the particularly low level of ice porosity that is obtained for Test 1. An interpretation for this case is that the ice thickness is so small and consequently the wave attenuation is so weak (as indicated by the low attenuation rates in Fig. 3a) that the CGG model views it as equivalent to a configuration with pack ice (corresponding to the limit $\beta \to 0$). This is consistent with the parameter values $\epsilon = 0.34, 0.94$ and 0.85 estimated from the SRCJ fits for Test 1, 2 and 3 as reported by Sutherland et al. (2019). These authors also tested their viscous model against the laboratory experiments of Newyear and Martin (1997), Wang and Shen (2010a) and Zhao and Shen (2015), and found the parameter ϵ to be smallest for Test 1 of Zhao and Shen among all the cases considered. We obtain a similar result here, with β being smallest for that particular experiment. Moreover, the set of $\beta = \{0.01, 0.07, 0.06\}$ seems to follow a pattern of variation similar to that for the set of $\epsilon = \{0.34, 0.94, 0.85\}$. Again, for such low levels of ice porosity as given by the CGG fit, the associated pore sizes $a = \{2.0, 4.8, 8.5\}$ cm may be deemed compatible with the typical ice diameters $\ell = \{3, 5, 20\}$ cm observed in Zhao and Shen (2015) for Test 1, 2, 3.

We point out in passing that Sutherland et al. (2019) set $\Delta_0 = 1$ and determined ϵ by a linear least-squares fitting method. In the present study, we fit (7) to the experimental data by minimizing (6) with respect to both Δ_0 and ϵ, based on the approach described in Section 2. This produces values of Δ_0 near 1 and values of ϵ that are very close to those reported in Sutherland et al. (2019), which may serve as evidence for the effectiveness of our fitting method. From the SRCJ fit shown in Fig. 3, we find $(\Delta_0, \epsilon) = (0.96, 0.34), (0.97, 0.97)$ and $(0.94, 0.82)$ for Test 1, 2 and 3.

Zhao and Shen (2015) also used their laboratory data to test the WS model and estimate such parameters as the shear modulus and kinematic viscosity. We will refer to their results as part of the discussion in Section 4.

3.4. Field observations of Wadhams et al. (1988)

During field operations in the Greenland and Bering Seas in the late 1970s and early 1980s, the Scott Polar Research Institute (Wadhams et al., 1988) carried out a series of experiments where wave attenuation was measured along a line of stations running from the open sea deep into an ice field. Large broken floes are a prominent feature of the ice field in this case. At each station, a wave buoy was inserted between floes to measure the local wave spectrum. A mean ice thickness was determined by coring at each of the experimental floes along the major axis of the incoming wave spectrum. Floe size distributions were derived from overlapping vertical photography from a helicopter. Among the measurements reported in Wadhams et al. (1988) (see their Table 2), we will use those from the Greenland Sea in 1979 and from the Bering Sea in 1983. Other data sets (e.g. 1978 Greenland Sea and 1979 Bering Sea) were deemed not suitable due to possibly larger experimental error or unwanted physical effects such as wave reflection/absorption from the fjords, as mentioned in Kohout and Meylan (2008). We will take this opportunity to compare with results of Kohout and Meylan (2008) (hereafter referred to as KM) who also tested their scattering model against these field observations.

An intriguing feature of the 1979 Greenland Sea and 1983 Bering Sea measurements is that they show a roll-over of attenuation rate as a function of wave period (or wave frequency), in lieu of a monotonic behavior. This roll-over occurs at short periods (or high frequencies) in the range considered. Continuum viscoelastic models or discrete scattering models have usually been unable to predict this phenomenon. Possible explanations that have been suggested include wind forcing, nonlinear wave interactions or instrument noise (Li et al., 2017; Perrie and Hu, 1996; Thomson et al., 2021; Wadhams et al., 1988). An exception that we are aware of in the context of linear theory is the three-layer viscoelastic model with eddy viscosity as recently proposed by Zhao and Shen (2018). Their numerical results show a roll-over
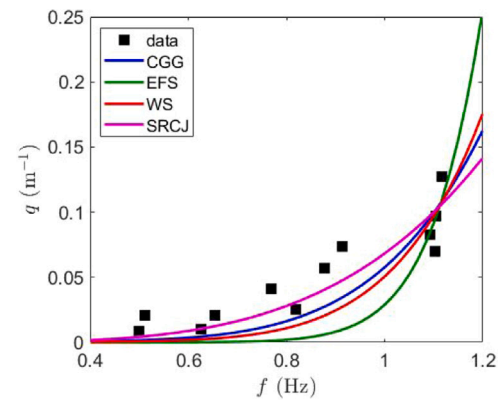
(a) $h = 2.5$ cm
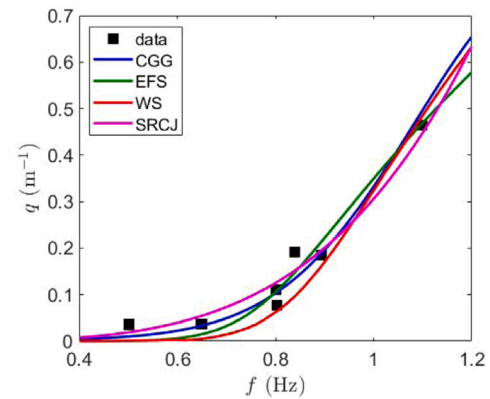
(b) $h = 4.0$ cm
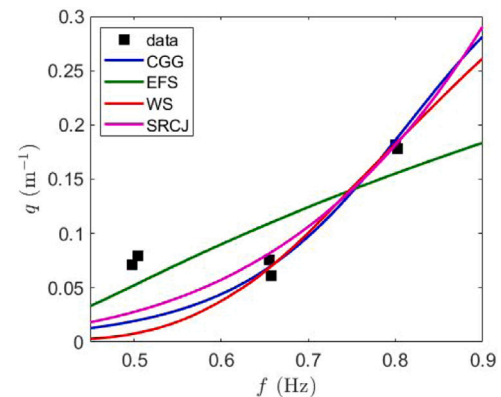
(c) $h = 7.0$ cm

Fig. 3. Comparison of attenuation rate vs. frequency between model predictions and laboratory data from Zhao and Shen (2015). Predictions from the CGG, EFS, SRCJ and WS models are shown. Laboratory data for (a) $h = 2.5$ cm (test 1, frazil/pancake ice), (b) $h = 4.0$ cm (test 2, pancake ice), (c) $h = 7.0$ cm (test 3, fragmented ice) are presented.

that accentuates as the thickness of the turbulent boundary layer (located between the viscoelastic ice layer and the inviscid water layer) increases. However, no comparison with field data featuring the roll-over was presented in that study. A similar phenomenon was observed by Liu et al. (1991) based on a linear model for a thin elastic plate with eddy viscosity (Liu and Mollo-Christensen, 1988). These authors derived a temporal rate of wave attenuation and converted it to a spatial rate by dividing it by the group velocity. As noted in Li et al.
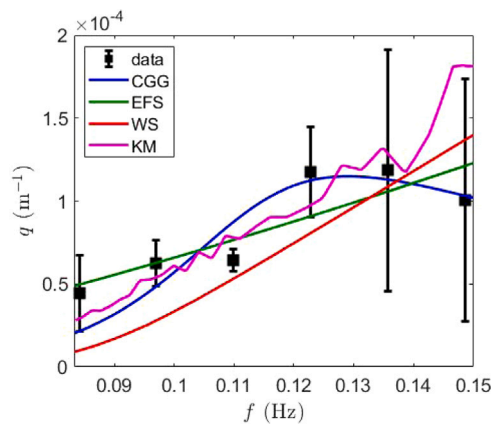
Fig. 4. Comparison of attenuation rate vs. frequency between model predictions and data for a broken floe field from the Greenland Sea 10 September 1979 experiment in Wadhams et al. (1988). Predictions from the CGG, EFS, KM and WS models are shown. Results for $h = 3.1$ m and $H = 1500$ m are presented.

(2017), this temporal rate is a monotonic function of frequency and so the fact that the spatial rate exhibits roll-over is likely due to the group velocity being non-monotonic and reaching a minimum at some frequency (Guyenne and Părău, 2012). Therefore, it is not clear from this result whether the roll-over effect is an intrinsic feature of the thin-plate viscoelastic model or is simply an artifact of the observation procedure.

3.4.1. Greenland Sea, 10 September 1979

During this experiment, the ice cover was sparse and the floes were generally large. The ice concentration was estimated to be $C = 0.17$ from photograph analysis. Because ice thicknesses could not be determined on that day and were not reported, we choose $h = 3.1$ m following Kohout and Meylan (2008) who suggest using the floe thickness from the 1978 data, which was based on 14 measurements through smooth areas. We set $H = 1500$ m (average depth of the Greenland Sea) and, for the CGG model, we assign the value $\beta = 1 - C = 0.83$ to ice porosity.

Note that the field measurements under consideration are on the wave spectrum, which is proportional to the square of the wave amplitude. Accordingly, we halve the corresponding decay rates when comparing to theoretical predictions for the wave amplitude. We see in Fig. 4 that the CGG model fits the field observations well, despite the small number of data points available. Among all the models at play, it is the only one that is able to reproduce some roll-over of q, with a peak near $f = 0.13$ Hz. In fairness, we should mention that experimental errors are more appreciable at this end of the spectrum. The CGG model also captures the stronger decay of attenuation rate at lower frequencies, although its predictions of q tend to be even lower than the measured values in the limit $f \to 0$. By contrast, the EFS and WS curves are monotonically increasing with f, almost linearly over the range of frequencies considered. The SRCJ fit is also found to be monotonically increasing with frequency and is not plotted in this figure.

Instead, we show the KM fit which is extracted from Fig. 8 in Kohout and Meylan (2008) (with appropriate rescaling to convert the dimensionless energy rates per floe number in that figure to dimensional rates of spatial attenuation for the wave amplitude). We point out that the KM model is a scattering model and is of different nature from the continuum formulation that is highlighted in the present study. It is thus not further discussed here and the reader is directed to Kohout and Meylan (2008) for more detail. Because scattering is believed to be the dominant mechanism for wave attenuation in broken floe fields, the KM model serves as a suitable independent reference for the comparison

with field observations from Wadhams et al. (1988). The KM curve appears to be rougher than the other theoretical curves, as it represents the average of 100 simulations with different random realizations of the floe size distribution. We can nonetheless discern a general trend that is monotonically increasing with frequency, and is approximately linear with a slope close to that of the WS curve.

The CGG fit presented in Fig. 4 returns a pore size $a = 14.6$ m. While it is difficult to give a physical interpretation for this parameter from the viewpoint of effective medium theory, we may associate it to a characteristic horizontal size of open-water areas in the context of an extensive broken floe field. It is reassuring that we find a value of a which is significantly larger than those obtained for the (smaller-scale) laboratory experiments of Wang and Shen (2010a) and Zhao and Shen (2015). Moreover, although pore size in the CGG model does not signify floe size as mentioned earlier (and these two parameters are not necessarily correlated), we deem it consistent that the estimated value $a = 14.6$ m is somewhat comparable in order of magnitude to the typical floe size ($\ell = 50$–80 m) observed on this expedition, as reported in Kohout and Meylan (2008).

3.5. Bering Sea, 7 February 1983

This experiment was carried out as part of the MIZEX West study in 1983. Following Perrie and Hu (1996) and Kohout and Meylan (2008), we take representative values for the ice concentration and thickness in this case to be $C = 0.72$ and $h = 1.5$ m, respectively. The ice cover was thus less fragmented than in the previous environment. We select $H = 1500$ m for the average depth of the Bering Sea and prescribe $\beta = 1 - C = 0.28$ in the CGG model.

As shown in Fig. 5, the roll-over is even more apparent here than in the previous observations due to the larger number of data points and smaller experimental errors. Overall, the same comments as in the previous section can be made on the comparison between the measurements and predictions. The CGG model can somewhat reproduce the roll-over of q near $f = 0.13$ Hz, despite the fact that the corresponding fit appears smoother in this region. It underestimates the peak amplitude and slightly overshoots the peak frequency. Interestingly, these relative features of the roll-over from the field observations and numerical estimates are reminiscent of the comparison given in Liu et al. (1991) (see their Fig. 13) between their viscoelastic theory and the same Bering Sea data. Note that attenuation rate is plotted as a function of wave period rather than frequency in their Fig. 13, where the roll-over takes place at short periods. At the opposite end of the spectrum, the CGG fit is also found to provide a good approximation for the low-frequency tail.

We see again in Fig. 5 that none of the other models produce a roll-over. The associated curves are all monotonically increasing with frequency, and look similar to those in Fig. 4, although they seem to display a more convex shape here. This convexity is especially pronounced for the KM and WS curves (the former is extracted from Fig. 11 in Kohout and Meylan, 2008). Notice again that the KM curve is rougher than the other curves for the same reason as mentioned earlier.

In comparison to these field data, the pore size deduced from the CGG fit turns out to be $a = 22.0$ m, which is not so different from the previous prediction ($a = 14.6$ m) for the Greenland Sea experiment. Given the denser floe field here, we might have expected a smaller pore size, nevertheless this value $a = 22.0$ m is definitely larger than those found for the frazil/pancake ice covers generated in the laboratory experiments of Wang and Shen (2010a) and Zhao and Shen (2015). It is striking how close this estimated pore size is to the floe diameter $\ell = 14.5$ m that was assumed by Perrie and Hu (1996) in their simulations of the Bering Sea observations.
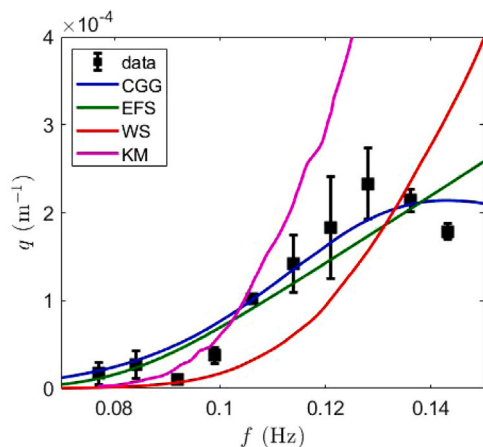
Fig. 5. Comparison of attenuation rate vs. frequency between model predictions and data for a broken floe field from the Bering Sea 7 February 1983 experiment in Wadhams et al. (1988). Predictions from the CGG, EFS, KM and WS models are shown. Results for $h = 1.5$ m and $H = 1500$ m are presented.
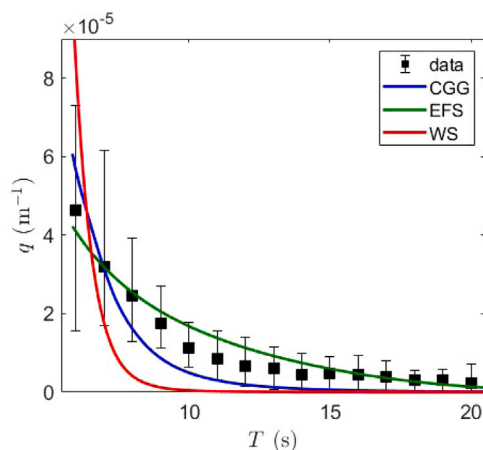

Fig. 6. Comparison of attenuation rate vs. period between model predictions and data for a broken floe field from the Antarctic MIZ (Kohout et al., 2014; Meylan et al., 2014). Predictions from the CGG, EFS and WS models are shown. Results for $h = 1$ m and $H = 4300$ m are presented.

Although it is difficult to discriminate any specific physical mechanism from the CGG formulation, which would be responsible for the observed roll-over, we recall preliminary results from Chen et al. (2019) suggesting that the relative motion between different constituents of the ice cover induces friction that may interfere with other (bulk) dissipative effects to help produce this non-monotonic behavior of the attenuation rate. As can be seen from the definition (2) of its controlling parameter b, this phenomenon in the CGG view is directly linked to the porous (hence heterogeneous) nature of the ice cover. Details of the frictional process are unclear in this effective medium approach and so we prefer not to attempt to interpret it further at this point. We have confirmed the previous presumption by fitting the CGG model to the Bering and Greenland Seas data in the absence of frictional effects (i.e. with b manually set to zero). No roll-over has emerged from these computations (this is not shown here for convenience); the CGG curve would be monotonically increasing with frequency and would look similar to the WS curve.

3.6. Field observations of Kohout et al. (2014)

We turn our attention to a more recent data set that was collected in the Antarctic MIZ as part of the Australian Antarctic Division's second Sea Ice Physics and Ecosystem Experiment in 2012 (Kohout and Williams, 2012). Wave measurements were made simultaneously using contemporary sensors at up to five locations on a transect spanning up to 250 km. Kohout et al. (2014) provided a preliminary report on these measurements to support the claim that wave activity and ice extent are correlated. A spectral analysis of the data was performed by Meylan et al. (2014) who examined in particular the dependence of attenuation rates on wave periods.

Following Mosig et al. (2015), we assume $h = 1$ m and $H = 4300$ m for our computations in this setting. Four estimates of mean ice concentration $C = 0.210, 0.481, 0.498, 0.576$ in areas of the Antarctic MIZ where the wave sensors drifted, are given in Meylan et al. (2014). These estimates were calculated using Nimbus-7 scanning multichannel microwave radiometer and Defense Meteorological Satellite Program (DMSP) Special Sensor Microwave/Imager Sounder (SSMIS) Passive Microwave Data. As a representative value, we specify the average $\beta = 0.56$ of the corresponding ice porosities in the CGG model. A camera installed on the upper deck of the ship monitored the floe size distribution during this expedition. Photographs of the broken floe field taken by this camera can be seen in Meylan et al. (2014).

Attenuation rates extracted from Fig. 8 in Mosig et al. (2015) (see also Fig. 4 in Meylan et al., 2014) are now shown in Fig. 6 and compared to theoretical predictions. Again, we take into account the difference between data on wave energy decay from Meylan et al. (2014) and estimates on wave amplitude decay from the various models by halving the former decay rates. For this particular data set, we plot q as a function of T (wave period) rather than f (wave frequency), as originally presented in Meylan et al. (2014) and Mosig et al. (2015), to retain a uniform resolution over the range of periods considered. Unlike the field observations discussed in the previous section, no roll-over is discernible from the data points in Fig. 6. Accordingly, none of the models involved in this comparison (including the CGG model) predict such a phenomenon; their fitting curves are all monotonically decreasing with increasing T.

Here the EFS model provides the closest fit as indicated in Fig. 6. The agreement is especially good at long periods while, as $T \to 0$, this model tends to underestimate the attenuation rate. Note that our version of the EFS curve bears a resemblance to the original one shown in Mosig et al. (2015) (see their Fig. 8), which may be viewed as further evidence for the effectiveness of our fitting procedure. By contrast, the CGG and WS curves are steeper, falling down more quickly as T increases. These two models produce negligible values of q at long periods, which are distinctly lower than the field data over most of the time interval being probed. On the other hand, they tend to overestimate the decay rates at short periods. Despite these discrepancies, the CGG fit is seen to lie within or near experimental error, while the WS fit tends to lie further below. We remark in passing that the decay rates observed in this case and in the Arctic MIZ (Wadhams et al., 1988) are significantly lower than those measured in the laboratory experiments as discussed earlier. This supports a previous statement from Section 2 that the decay rates in frazil/pancake ice can be several orders of magnitude greater than in a broken floe field (e.g. compare values of q between Figs. 2 and 6).

The pore size returned by the CGG fit to these field measurements is $a = 72.0$ m, which is larger than the predictions for the two previous data sets from the Arctic MIZ. While the photographs in Meylan et al. (2014) might suggest a lower value of a for this broken floe field, we point out that these were taken immediately after deployment of the sensors. Over the duration of their operation, these sensors tended to drift into open ocean, as mentioned in Meylan et al. (2014). Furthermore, considering that the MIZ explored was overall more on the sparse side ($\beta = 0.56$), with dominant floe sizes ℓ ranging from a few meters to greater than 100 m in the various areas visited by the sensors, we deem the pore size $a = 72.0$ m estimated from the CGG model to be reasonable here as well.
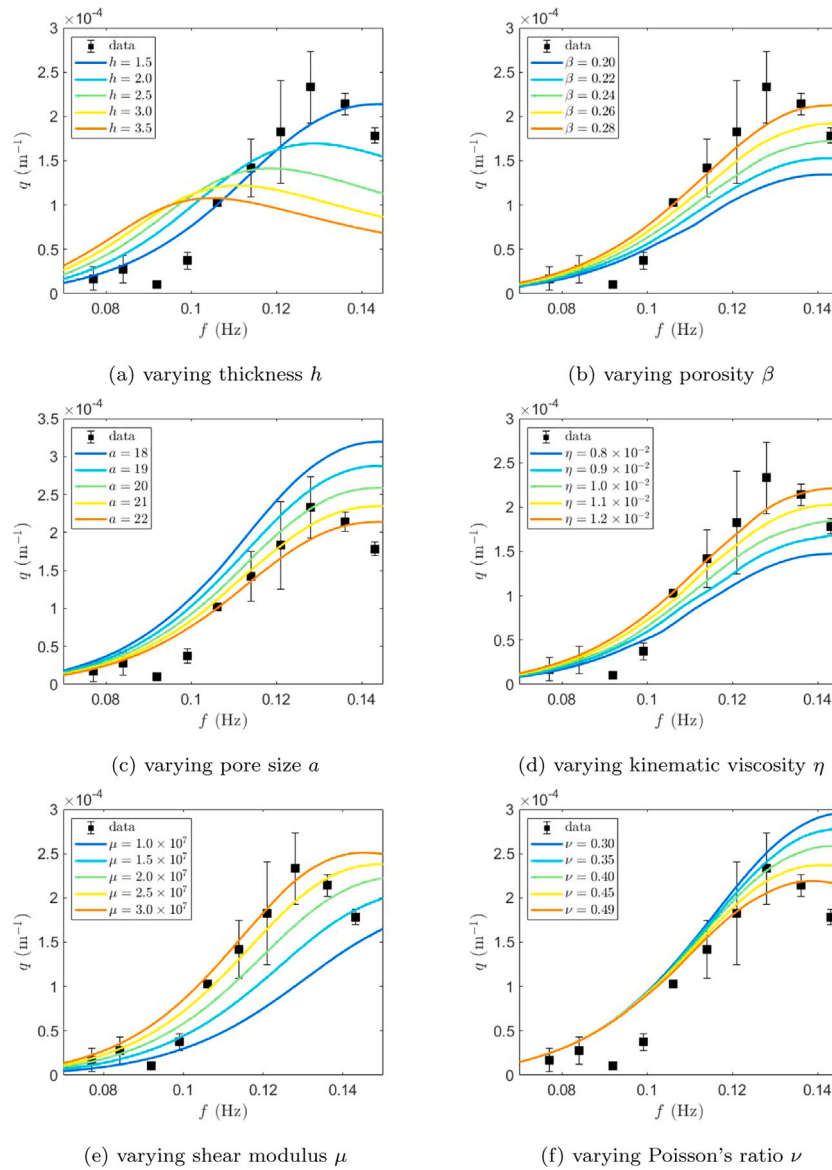
Fig. 7. Sensitivity of attenuation rate vs. frequency to varying parameters as predicted by the CGG model. Data for a broken floe field from the Bering Sea 7 February 1983 experiment (Wadhams et al., 1988) are considered. Results for varying (a) thickness h (m), (b) porosity β, (c) pore size a (m), (d) kinematic viscosity η (m^2 s^{-1}), (e) shear modulus μ (Pa), (f) Poisson's ratio ν are presented.

Table 1

Estimates of shear modulus and kinematic viscosity from the CGG, EFS and WS fits to data on attenuation rate for the various cases under consideration. Values of shear modulus are normalized relative to $\mu_0 = 10^9$ Pa, while values of kinematic viscosity are normalized relative to $\eta_0 = 10^{-2}$ m^2 s^{-1}. Lowest estimates are highlighted in red while highest estimates are highlighted in blue.

Experiment	Data set	CGG model		EFS model		WS model	
		μ ($\times 10^9$) (Pa)	η ($\times 10^{-2}$) (m^2 s^{-1})	μ ($\times 10^9$) (Pa)	η ($\times 10^{-2}$) (m^2 s^{-1})	μ ($\times 10^9$) (Pa)	η ($\times 10^{-2}$) (m^2 s^{-1})
Newyear & Martin	Test 1	5.00×10^{-7}	7.52	1.17×10^{-7}	2.50	**6.40×10^{-11}**	2.80
	Test 2	6.00×10^{-7}	9.00	1.26×10^{-7}	2.64	1.20×10^{-10}	3.76
Wang & Shen	Tank 2	1.82×10^{-4}	**1.22×10^{-2}**	4.80×10^{-4}	2.25×10^4	1.15×10^{-6}	9.61
	Tank 3	1.73×10^{-4}	4.00×10^{-2}	2.80×10^{-5}	1.20×10^3	4.00×10^{-7}	5.10
Zhao & Shen	Test 1	7.34×10^{-6}	8.32×10^{-2}	7.20×10^{-6}	8.00×10^2	4.20×10^{-9}	1.46
	Test 2	4.21×10^{-5}	4.68×10^{-2}	9.40×10^{-4}	1.62×10^4	2.47×10^{-4}	4.50×10^3
	Test 3	1.44×10^{-4}	9.22×10^{-2}	7.20×10^{-2}	1.44×10^6	8.32×10^{-4}	1.32×10^4
Wadhams et al.	Greenland Sea	1.38×10^{-2}	7.00×10^{-2}	**6.50×10^2**	**4.62×10^9**	6.75×10^{-2}	1.14×10^5
	Bering Sea	3.30×10^{-2}	1.16	1.54	5.28×10^6	4.00×10^{-2}	2.00×10^5
Kohout et al.	Antarctic MIZ	1.58×10^{-2}	1.00	4.20×10^2	4.20×10^8	6.00×10^{-3}	1.20×10^4

4. Discussion on shear modulus and kinematic viscosity

We further check the performance of the CGG model by comparing its estimates of shear modulus μ and kinematic viscosity η with predictions by the EFS and WS models. These two parameters are important measures of effective viscoelastic properties of the ice cover and are common to all three continuum formulations. Such an assessment would be suitable as part of the calibration of these models in view of potential applications to large-scale wave forecasting in the polar regions. Similar parametric calibration of the EFS and WS models has been conducted in Cheng et al. (2017), Mosig et al. (2015) and Zhao and Shen (2015), although these studies used different methods to fit the theoretical predictions to experimental data.

Table 1 lists values of μ and η as determined from the CGG, EFS and WS fits to the laboratory experiments and field observations that we discussed in the previous sections. To highlight the effective character of these models as applied to wave propagation in various ice-cover types, these estimates are presented in such a way that they are normalized relative to typical values $\mu \simeq \mu_0 = 10^9$ Pa for pack ice (Mosig et al., 2015; Williams and Francois, 1992) and $\eta \simeq \eta_0 = 10^{-2}$ m^2 s^{-1} for grease or pancake ice (Doble et al., 2015; Newyear and Martin, 1999). As alluded to in Section 2, Table 1 confirms that both parameters can take a wide range of values depending on the particular model and ice conditions. Among all the cases considered, the highest values of μ and η are both achieved by the EFS fit to the Greenland Sea observations (Wadhams et al., 1988). The lowest value of μ is given by the WS fit to the laboratory Test 1 of Newyear and Martin (1997). The lowest value of η is returned by the CGG fit to the Tank 2 experiment of Wang and Shen (2010a). These extreme values are highlighted in blue (highest) and red (lowest) in Table 1. As expected, for all three models, the shear modulus μ (which is a measure of the ice-cover's elasticity) is found to be smallest for grease ice (Test 1 in Newyear and Martin, 1997) and largest for a broken floe field (Arctic MIZ Wadhams et al., 1988). Their estimates of μ for both Antarctic and Arctic MIZ remain overall within two orders of magnitude from the typical value μ_0 for pack ice. By contrast, the kinematic viscosity η (which may represent a combination of various attenuating effects in this continuum framework) exhibits a more complicated behavior depending on the particular model and ice conditions. We point out however that all three models predict η to be on the order of η_0 for the grease-ice experiments (Newyear and Martin, 1997), which is consistent with values $\eta = 2$–$3\,\eta_0$ inferred by Newyear and Martin (1999) who fitted data from Newyear and Martin (1997) to Keller's two-layer viscous model (Keller, 1998). For a broken floe field, the viscosity estimates from both EFS and WS models are found to be larger by several orders of magnitude than their counterparts for grease ice. On the other hand, the corresponding predictions from the CGG model remain comparable between these two types of ice cover.

On a related note, we see that μ and η as determined by the CGG fit only vary over 6 and 3 orders of magnitude respectively, among all the cases considered. By contrast, μ and η as predicted by the WS fit vary over 10 and 6 orders of magnitude respectively, while both parameters in the EFS model vary over 10 orders of magnitude. This suggests that both μ and η in the CGG model may only require moderate tuning in view of potential applications to operational wave forecasting. For both CGG and WS models, the order of magnitude of μ tends to exhibit more scatter than that of η. Recognizing that the CGG and WS models provide a more refined representation (two-layer formulation) of the ice cover as opposed to the EFS model, and given that μ is an important measure of elastic properties, this distinction observed between μ and η may be explained by the fact that a wide range of ice conditions (spanning laboratory experiments and field observations) is examined in the present study.

Our estimates of μ (4.2×10^{11} Pa) and η (4.2×10^6 m^2 s^{-1}) from the EFS fit to the Antarctic MIZ data are consistent with those reported in Mosig et al. (2015) for the same model ($\mu = 4.9 \times 10^{12}$ Pa, $\eta = 5.0 \times 10^7$ m^2 s^{-1}). Both of them are several orders of magnitude larger than the reference values μ_0 and η_0 (especially for η). Regardless of how close the fit is, the EFS model tends to require very large values of these parameters in order to reproduce wave attenuation in broken floe fields of the Antarctic and Arctic MIZ. This may be interpreted as a way to make up for the thin-plate approximation so that elastic properties of the ice cover would be sufficiently well captured in these situations. Recalling the good agreement obtained by the SRCJ fit to laboratory data of Zhao and Shen (2015) (Section 3.3) and by the EFS fit to Antarctic MIZ data (Section 3.6), our results suggest that simple models like EFS or SRCJ (with few parameters) may be successful at fitting experimental data, especially for data sets showing a monotonic trend. However, their rheological parameters may be required to take extreme values as indicated here, or these models may be unable to describe more complex phenomena such as a roll-over in other situations.

Our estimates of μ ($\{4.2, 2.5 \times 10^5, 8.3 \times 10^5\}$ Pa) and η ($\{1.5 \times 10^{-2}, 45.0, 131.6\}$ m^2 s^{-1}) from the WS fit to the laboratory measurements of Zhao and Shen (2015) are in good agreement with their own findings ($\mu = \{21, 5 \times 10^5, 1 \times 10^6\}$ Pa, $\eta = \{1.4 \times 10^{-2}, 61, 140\}$ m^2 s^{-1}) for Test 1, 2, 3 respectively (see their Table 2). These authors also fitted the WS model to a data set from Wang and Shen (2010a) (it was not clearly stated which experiment was considered) and obtained $\mu = 48$ Pa, $\eta = 4 \times 10^{-2}$ m^2 s^{-1} which again are fairly close in terms of order of magnitude to our own results ($\mu = \{1.1 \times 10^3, 4.0 \times 10^2\}$ Pa, $\eta = \{9.6 \times 10^{-2}, 5.1 \times 10^{-2}\}$ m^2 s^{-1}) for Tank 2 and 3 respectively. When examining the CGG and WS models against the field observations, we see that their predictions of μ are comparable to each other on the order of 10^7 Pa, which contrasts with the much higher values from the EFS fit, as noted above. This similarity however does not extend to η since the WS model yields values that are higher than the CGG predictions by several orders of magnitude. Again, the range of estimated η from the CGG fit is strikingly narrow among all the cases considered, in comparison to the other two models.

It is also worth mentioning that the estimates $\mu = 3.3 \times 10^7$ Pa and $\eta = 1.2 \times 10^{-2}$ m^2 s^{-1} from the CGG fit to the Bering Sea measurements are consistent with those ($\mu = 2.3 \times 10^9$ Pa, $\eta = 1.5 \times 10^{-2}$ m^2 s^{-1}) reported in Liu et al. (1991) for the same data set. As stated earlier, these authors used a thin-plate viscoelastic model and were able to emulate the roll-over phenomenon to some extent (see their Fig. 13). In that study, μ was assigned a typical value $\sim \mu_0$ for pack ice while η was deduced from the data fitting. Interestingly, the fitting curve shown in Fig. 13 of Liu et al. (1991) bears a resemblance to the CGG curve in our Fig. 5 (modulo the switch between wave frequency and period for the horizontal axis). Lastly, we remark that the CGG predictions of $\eta \sim 10^{-2}$–$10^0\,\eta_0$ for the data sets from the Antarctic and Arctic MIZ are encouraging in view of earlier measurements that reported values of eddy viscosity under large ice floes, ranging from 2.4×10^{-3} m^2 s^{-1} in the central Arctic Ocean (Hunkins, 1966) to 2.1×10^{-2} m^2 s^{-1} in the Weddell Sea (Antarctic MIZ) (McPhee and Martinson, 1994).

5. Sensitivity tests

Given the rather large number of rheological parameters associated with the ice cover in the CGG formulation, it is of interest to check their individual relevance to this problem and test the sensitivity of attenuation rate predictions with respect to these parameters. For this purpose, we take the Bering Sea observations as a representative discriminating case because it exhibits unusual features such as the roll-over phenomenon and contains a fair number of data points. We focus our attention on the following parameters: h (thickness), β (porosity), a (pore size), η (kinematic viscosity), μ (shear modulus) and ν (Poisson's

ratio). As alluded to in previous sections, some of them which are related to geometrical features of the ice cover (e.g. thickness, porosity, pore size) may be estimated by in-situ measurement or remote sensing, while others which are related to material properties (e.g. kinematic viscosity, shear modulus) would be more difficult to determine or guess. With this in mind, a sensitivity analysis may help assign predefined values to some of these parameters (as opposed to other parameters that may require more tuning), in order to reduce the parameter space for the CGG model.

For each of these parameters, Fig. 7 displays a set of curves for the attenuation rate as predicted by the CGG model. The reference regime of parameters is given by the corresponding best fit to the Bering Sea data, as discussed in the previous section (see Fig. 5). This set of curves is obtained by varying the parameter under consideration while freezing the other parameters at their original best-fitting values. The objective of such an analysis is to examine how perturbations in individual parameters would affect the original best fit. The range of perturbations for each parameter is chosen to be an interval around its best-fitting value.

Ice thickness is a distinctive feature of the ice cover in the CGG formulation, as opposed to the viewpoint in the thin-plate approximation. Fig. 7(a) reveals that the roll-over tends to shift upward and to higher frequencies as h is decreased. This tendency is quite pronounced and suggests strong sensitivity of q with respect to h. A decrease in h by a factor of 3 shifts the peak outside the frequency range of the experimental data, and moves it out of sight in this figure. The fact that shorter waves (i.e. at higher frequencies) experience more attenuation in thinner ice (i.e. for smaller h), which is rather counter-intuitive, is reminiscent of a common feature in models for water waves over seabed composed of a viscous mud layer, where dissipation has a non-monotonic dependence on mud-layer thickness, with thicker layers being less dissipative (Chen et al., 2019; Collins et al., 2017; Dalrymple and Liu, 1978). Ice porosity and pore size are rheological parameters that are characteristic of the present model. As illustrated in Figs. 7(b) and (c), increasing β or decreasing a has the basic effect of raising the attenuation rate and accentuating the roll-over. In either case, the peak remains around $f = 0.13$ Hz as β or a is varied. Note that the dichotomy in variation between β and a is attributed to their contrasting roles in the friction process. Because the parameter b depends linearly on β while it is inversely proportional to a^2 according to (2), friction is thus enhanced (and so is the roll-over) as β is increased or a is decreased. A similar behavior occurs as η is increased (see Fig. 7d), which is anticipated considering the linear dependence of b on η. A slightly more complicated picture is observed for the variation with respect to μ. Inspecting Fig. 7(e), the roll-over tends to shift upward and to lower frequencies as μ is increased. The sensitivity of q to ν is relatively weak and is confined to the high-frequency region, as suggested by Fig. 7(f). This explains why, for convenience and given that $0 < \nu < 1/2$, we set $\nu = 0.4$ in the previous computations (which is close to the typical value $\nu = 1/3$ for pack ice Williams and Francois, 1992).

Our sensitivity tests indicate that all these parameters have some influence on the roll-over, affecting its amplitude and/or position. Sensitivity of q with respect to h and μ seems to be most nontrivial, and is particularly strong for h. Liu et al. (1991) also concluded from their model-data comparison that the frequency at which the roll-over occurs depends on ice conditions, especially ice thickness. In light of this sensitivity analysis and results from Section 3, to help reduce the parameter space, it would also be reasonable to fix the pore size with some predefined value of order $O(10)$ m for potential applications to wave forecasting in the MIZ. This is even more relevant considering that this parameter only appears in the expression (2) of the friction coefficient for the CGG model.

6. Conclusions

To assess the recently proposed CGG model, we test it against a selection of laboratory experiments and field observations taken from the literature, concerning wave attenuation in sea ice. Altogether, these measurements span a wide range of ice conditions and wave frequencies. We fit the theoretical predictions to data on attenuation rate via error minimization, which in turn yields estimates for effective rheological parameters in addition to estimates for the attenuation rate. Whenever the information is available, the porosity parameter is assigned a value that is the complement of the mean ice concentration. To further check this model's performance, we also compare it to other existing viscoelastic theories under the same various conditions. Numerical solutions of the dispersion relations can be found using relatively simple selection criteria. As a byproduct, we independently recover (via a different fitting procedure) a number of results that are similar to those reported in previous studies. While the CGG system features a larger number of physical parameters than other existing viscoelastic formulations, our investigation suggests that some of these parameters may be assigned predefined values, or may be estimated by in-situ measurement or remote sensing.

Special attention is paid to the EFS and WS formulations which share some common features with the CGG system. For such parameters as μ (shear modulus) and η (kinematic viscosity) which control the viscoelastic properties, we find that the range of estimated values (over all the situations considered) may differ significantly from one model to another. Among these three representations, the CGG (resp. EFS) model turns out to be the one for which the predicted range of both μ and η is the narrowest (resp. widest) in orders of magnitude. Even for individual situations, this difference in parameter recovery may be considerable. As expected, for grease ice, all three models predict η on the order of $\eta_0 = 10^{-2}$ m^2 s^{-1} and μ to be essentially negligible compared to the typical value $\mu_0 = 10^9$ Pa for pack ice. On the other hand, for broken floe fields, there is more variability in the determination of these parameters, especially for η. We obtain in this case values of μ that may be lower (for CGG and WS) or higher (for EFS) than μ_0 by a few orders of magnitude. Estimates of η from the EFS and WS fits tend to be larger than η_0 by several orders of magnitude, while those from the CGG fit remain around this reference value. Overall, the CGG model provides good fits to the data on attenuation rate for the various cases under consideration.

Against the Antarctic MIZ data, the EFS counterpart appears to be a clear favorite, but the corresponding fit is achieved for values of μ and η that are both excessively high, a fact which has also been pointed out in Mosig et al. (2015). By contrast, the CGG fit returns markedly lower values for these parameters, with μ being lower than μ_0 by two orders of magnitude and η being essentially equal to η_0. In comparison to the Arctic MIZ data (from both the Bering and Greenland Seas), the CGG model is able to reasonably reproduce the roll-over of attenuation rate, unlike both EFS and WS counterparts which only predict a monotonic growth with frequency. According to the poroelastic formulation, this intriguing phenomenon is attributed to friction caused by the relative motion between fluid and solid components of the ice cover, which highlights the role of porosity in the present description of wave–ice interactions, as such friction is directly connected to the porous nature of the ice cover. This dissipative mechanism could possibly be a contributing factor in the roll-over effect as reported in field observations.

While the present results are encouraging, further calibration and validation are needed in order to determine the extent to which the CGG model is applicable. The current version has limitations, in particular it is linear and two-dimensional. It would be suitable to compare with more recent measurements from the Arctic MIZ as in Cheng et al. (2017) and de Santi et al. (2018) where previous viscous or viscoelastic models were tested. Using such data requires substantial processing and analysis to extract the apparent attenuation rate from directional wave spectra. Because the fitting procedure in Cheng et al. (2017) and de Santi et al. (2018) is based on minimizing an objective function similar to (6), and considering the overall good agreement found in the present study, we expect the CGG model to perform satisfactorily in comparison with those data sets as well.

In the future, it would be of interest to extend these results to the three-dimensional setting (for wave propagation in two horizontal directions) as well as to the nonlinear case. Discrepancies that we have observed may partly be attributed to such effects. Nonlinear theory of wave–ice interactions has drawn increasing attention in recent years (Dinvay et al., 2019; Guyenne and Pǎrǎu, 2012, 2014, 2017).

Declaration of competing interest

The authors declare that they have no known competing financial interests or personal relationships that could have appeared to influence the work reported in this paper.

Appendix. Coefficients in the dispersion relation

Coefficients in the dispersion relation (1) have the following expressions:

$$
\begin{aligned}
T_1 = {}& 2E_1 E_{12}[E_2 E_{23}(1 - \cosh(D_1 h)\cosh(D_3 h))\sinh(D_2 h) \\
& - E_1 E_{13}(1 - \cosh(D_1 h)\cosh(D_2 h))\sinh(D_3 h)] \\
& + \sinh(D_1 h)[2E_1 E_{13} E_2 E_{23}(-1 + \cosh(D_2 h)\cosh(D_3 h)) \\
& - (E_1^2(E_{12}^2 + E_{13}^2) + E_2^2 E_{23}^2)\sinh(D_2 h)\sinh(D_3 h)] ,
\end{aligned}
$$

$$
\begin{aligned}
T_2 = {}& E_1[(E_{17} E_4 E_7 + E_{18} E_6 E_9)(1 - \cosh(D_1 h)\cosh(D_2 h)) \\
& - (E_{14} E_2 E_{21} E_7 - E_{20} E_5 E_9)(1 - \cosh(D_1 h)\cosh(D_3 h)) \\
& - (E_{19} E_4 E_5 - E_{14} E_2 E_{22} E_6)(1 - \cosh(D_2 h)\cosh(D_3 h))] \\
& - E_1[(E_{17} E_3 E_7 + E_{18} E_6 E_8)(1 - \cosh(D_1 h)\cosh(D_2 h))\cosh(D_3 h) \\
& + (E_{16} E_2 E_{21} E_7 - E_{20} E_5 E_8)\cosh(D_2 h)(-1 + \cosh(D_1 h)\cosh(D_3 h)) \\
& + (E_{19} E_3 E_5 - E_{16} E_2 E_{22} E_6)\cosh(D_1 h)(-1 + \cosh(D_2 h)\cosh(D_3 h))] \\
& + E_1(E_{12} E_4 E_6 + E_{13} E_7 E_9)\sinh(D_1 h)\sinh(D_2 h) \\
& - E_1(E_{12} E_3 E_6 + E_{13} E_7 E_8)\cosh(D_3 h)\sinh(D_1 h)\sinh(D_2 h) \\
& + (E_1^2 E_{12} E_{14} E_5 - E_2 E_{23} E_7 E_9)\sinh(D_1 h)\sinh(D_3 h) \\
& - (E_1^2 E_{12} E_{16} E_5 - E_2 E_{23} E_7 E_8)\cosh(D_2 h)\sinh(D_1 h)\sinh(D_3 h) \\
& - (E_1^2 E_{13} E_{14} E_5 - E_2 E_{23} E_4 E_6)\sinh(D_2 h)\sinh(D_3 h) \\
& + (E_1^2 E_{13} E_{16} E_5 - E_2 E_{23} E_3 E_6)\cosh(D_1 h)\sinh(D_2 h)\sinh(D_3 h) ,
\end{aligned}
$$

$$
\begin{aligned}
T_3 = {}& E_1[(E_{11} E_{18} E_6 + E_{10} E_{17} E_7)(1 - \cosh(D_1 h)\cosh(D_2 h))\cosh(D_3 h) \\
& - (E_{11} E_{20} E_5 - E_{15} E_2 E_{21} E_7)\cosh(D_2 h)(-1 + \cosh(D_1 h)\cosh(D_3 h)) \\
& + (E_{10} E_{19} E_5 - E_{15} E_2 E_{22} E_6)\cosh(D_1 h)(-1 + \cosh(D_2 h)\cosh(D_3 h))] \\
& + E_1(E_{10} E_{12} E_6 + E_{11} E_{13} E_7)\cosh(D_3 h)\sinh(D_1 h)\sinh(D_2 h) \\
& + (E_1^2 E_{12} E_{15} E_5 - E_{11} E_2 E_{23} E_7)\cosh(D_2 h)\sinh(D_1 h)\sinh(D_3 h) \\
& - (E_1^2 E_{13} E_{15} E_5 - E_{10} E_2 E_{23} E_6)\cosh(D_1 h)\sinh(D_2 h)\sinh(D_3 h) ,
\end{aligned}
$$

and the E_j ($j = 1, \dots, 23$) are defined as follows:

$$
\begin{aligned}
E_1 = {}& 2D_3 \kappa^2 \mu_c , \\
E_2 = {}& -(D_2^2 - \kappa^2)(F_6 Q + F_8 R)(-\kappa^2(F_7 Q \\
& + F_5 \lambda) + D_1^2(F_7 Q + F_5(\lambda + 2\mu_c))) \\
& + (D_1^2 - \kappa^2)(F_5 Q + F_7 R)(-\kappa^2(F_8 Q \\
& + F_6 \lambda) + D_2^2(F_8 Q + F_6(\lambda + 2\mu_c))) , \\
E_3 = {}& -(D_2^2 - \kappa^2)(F_6 Q + F_8 R)(\rho_s - \rho_f)(1 - \beta) , \\
E_4 = {}& -(D_2^2 - \kappa^2)(F_6 Q + F_8 R)\rho_s(1 - \beta) \\
& + \rho_f \beta[-\kappa^2(F_8 Q + F_6 \lambda) + D_2^2(F_8 Q + F_6(\lambda + 2\mu_c))] , \\
E_5 = {}& -2D_1 D_2 F_6(F_5(-1 + \beta) - F_7 \beta) + 2D_1 D_2 F_5(F_6(-1 + \beta) - F_8 \beta) , \\
E_6 = {}& D_1(D_3^2 + \kappa^2)(F_5(-1 + \beta) - F_7 \beta) + 2D_1 F_5 \kappa^2(1 + (-1 + F9)\beta) , \\
E_7 = {}& D_2(D_3^2 + \kappa^2)(F_6(-1 + \beta) - F_8 \beta) + 2D_2 F_6 \kappa^2(1 + (-1 + F9)\beta) , \\
E_8 = {}& -(D_1^2 - \kappa^2)(F_5 Q + F_7 R)(\rho_s - \rho_f)(1 - \beta) , \\
E_9 = {}& -(D_1^2 - \kappa^2)(F_5 Q + F_7 R)\rho_s(1 - \beta) \\
& + \rho_f \beta[-\kappa^2(F_7 Q + F_5 \lambda) + D_1^2(F_7 Q + F_5(\lambda + 2\mu_c))] , \\
E_{10} = {}& -(D_2^2 - \kappa^2)(F_6 Q + F_8 R)\rho_f(1 - \beta) \\
& + \rho_f \beta[-\kappa^2(F_8 Q + F_6 \lambda) + D_2^2(F_8 Q + F_6(\lambda + 2\mu_c))] , \\
E_{11} = {}& -(D_1^2 - \kappa^2)(F_5 Q + F_7 R)\rho_f(1 - \beta) \\
& + \rho_f \beta[-\kappa^2(F_7 Q + F_5 \lambda) + D_1^2(F_7 Q + F_5(\lambda + 2\mu_c))] , \\
E_{12} = {}& 2D_1 F_5(D_2^2 - \kappa^2)(F_6 Q + F_8 R) , \\
E_{13} = {}& 2D_2 F_6(D_1^2 - \kappa^2)(F_5 Q + F_7 R) , \\
E_{14} = {}& \rho_f \beta , \\
E_{15} = {}& \rho_f \beta , \\
E_{16} = {}& 0 , \\
E_{17} = {}& 2D_1 F_5(D_1^2 - \kappa^2)(F_5 Q + F_7 R) , \\
E_{18} = {}& 2D_2 F_6(D_2^2 - \kappa^2)(F_6 Q + F_8 R) , \\
E_{19} = {}& (D_1^2 - \kappa^2)(D_3^2 + \kappa^2)(F_5 Q + F_7 R) , \\
E_{20} = {}& (D_2^2 - \kappa^2)(D_3^2 + \kappa^2)(F_6 Q + F_8 R) , \\
E_{21} = {}& 2D_1 F_5 , \\
E_{22} = {}& 2D_2 F_6 , \\
E_{23} = {}& D_3^2 + \kappa^2 .
\end{aligned}
$$

The expressions of λ, Q, R, D_j ($j = 1, 2, 3$) and F_j ($j = 1, \dots, 8$) in terms of wave parameters and rheological parameters can be found in Chen et al. (2019). The complex shear modulus μ_c is given by (5).

References

Ardhuin, F., Sutherland, P., Doble, M., Wadhams, P., 2016. Ocean waves across the arctic: Attenuation due to dissipation dominates over scattering for periods longer than 19 s. Geophys. Res. Lett. 43, 5775–5783.

Bennetts, L.G., Squire, V.A., 2012. On the calculation of an attenuation coefficient for transects of ice-covered ocean. Proc. R. Soc. Lond. Ser. A Math. Phys. Eng. Sci. 468, 136–162.

Chen, H., Gilbert, R.P., Guyenne, P., 2018. A Biot model for the determination of material parameters of cancellous bone from acoustic measurements. Inverse Problems 34, 085009.

Chen, H., Gilbert, R.P., Guyenne, P., 2019. Dispersion and attenuation in a porous viscoelastic model for gravity waves on an ice-covered ocean. Eur. J. Mech. B Fluids 78, 88–105.

Cheng, S., Rogers, W.E., Thomson, J., Smith, M., Doble, M.J., Wadhams, P., Kohout, A.L., Lund, B., Persson, O.P.G., C.O. Collins, III., Ackley, S.F., Montiel, F., Shen, H.H., 2017. Calibrating a viscoelastic sea ice model for wave propagation in the Arctic fall marginal ice zone. J. Geophys. Res. 122, 8770–8793.

Collins, C.O., Rogers, W.E., Lund, B., 2017. An investigation into the dispersion of ocean surface waves in sea ice. Ocean Dyn. 67, 263–280.

Craig, W., Guyenne, P., Sulem, C., 2009. Water waves over a random bottom. J. Fluid Mech. 640, 79–107.

Dalrymple, R.A., Liu, P.L.-F., 1978. Waves over soft muds: a two-layer fluid model. J. Phys. Oceanogr. 8, 1121–1131.

de Bouard, A., Craig, W., Diaz-Espinosa, O., Guyenne, P., Sulem, C., 2008. Long wave expansions for water waves over random topography. Nonlinearity 21, 2143–2178.

de Carolis, G., Desiderio, D., 2002. Dispersion and attenuation of gravity waves in ice: a two-layer viscous fluid model with experimental data validation. Phys. Lett. A 305, 399–412.

de Santi, F., de Carolis, G., Olla, P., Doble, M., Cheng, S., Shen, H.H., Wadhams, P., Thomson, J., 2018. On the ocean wave attenuation rate in grease-pancake ice, a comparison of viscous layer propagation models with field data. J. Geophys. Res. 123, 5933–5948.

Dinvay, E., Kalisch, H., Părău, E.I., 2019. Fully dispersive models for moving loads on ice sheets. J. Fluid Mech. 876, 122–149.

Doble, M.J., Bidlot, J.-R., 2013. Wave buoy measurements at the Antarctic sea ice edge compared with an enhanced ECMWF WAM: Progress towards global waves-in-ice modeling. Ocean Model. 70, 166–173.

Doble, M.J., de Carolis, G., Meylan, M.H., Bidlot, J.-R., Wadhams, P., 2015. Relating wave attenuation to pancake ice thickness, using field measurements and model results. Geophys. Res. Lett. 42, 4473–4481.

Fox, C., Squire, V.A., 1994. On the oblique reflexion and transmission of ocean waves at shore fast sea ice. Philos. Trans. R. Soc. Lond. A Math. Phys. Eng. Sci. 347, 185–218.

Guyenne, P., 2006. Large-amplitude internal solitary waves in a two-fluid model. C. R. Mec. 334, 341–346.

Guyenne, P., Părău, E.I., 2012. Computations of fully nonlinear hydroelastic solitary waves on deep water. J. Fluid Mech. 713, 307–329.

Guyenne, P., Părău, E.I., 2014. Finite-depth effects on solitary waves in a floating ice sheet. J. Fluids Struct. 49, 242–262.

Guyenne, P., Părău, E.I., 2017. Numerical study of solitary wave attenuation in a fragmented ice sheet. Phys. Rev. Fluids 2, 034002.

Hunkins, K., 1966. Ekman drift currents in the Arctic ocean. Deep Sea Res. 13, 607–620.

Keller, J.B., 1998. Gravity waves on ice-covered water. J. Geophys. Res. 103, 7663–7669.

Kohout, A.L., Meylan, M.H., 2008. An elastic plate model for wave attenuation and ice floe breaking in the marginal ice zone. J. Geophys. Res. 113, C09016.

Kohout, A.L., Williams, M.J.M., 2012. Waves-in-Ice Observations Made During the SIPEX II Voyage of the Aurora Australis. Tech. Rep., Australian Antarctic Data Centre, Hobart, Tasmania, Australia.

Kohout, A.L., Williams, M.J.M., Dean, S., Meylan, M.H., 2014. Storm-induced sea ice breakup and the implications for ice extent. Nature 509, 604–607.

Li, J., Kohout, A.L., Doble, M.J., Wadhams, P., Guan, C., Shen, H.H., 2017. Rollover of apparent wave attenuation in ice covered seas. J. Geophys. Res. 122, 8557–8566.

Liu, A.K., Holt, B., Vachon, P.W., 1991. Wave propagation in the marginal ice zone: model predictions and comparisons with buoy and synthetic aperture radar data. J. Geophys. Res. 96, 4605–4621.

Liu, A.K., Mollo-Christensen, E., 1988. Wave propagation in a solid ice pack. J. Phys. Oceanogr. 18, 1702–1712.

McPhee, M.G., Martinson, D.G., 1994. Turbulent mixing under drifting pack ice in the Weddell Sea. Science 263, 218–221.

Meylan, M.H., Bennetts, L.G., Kohout, A.L., 2014. In situ measurements and analysis of ocean waves in the Antarctic marginal ice zone. Geophys. Res. Lett. 41, 5046–5051.

Montiel, F., Squire, V.A., Bennetts, L.G., 2016. Attenuation and directional spreading of ocean wave spectra in the marginal ice zone. J. Fluid Mech. 790, 492–522.

Mosig, J.E., Montiel, F., Squire, V.A., 2015. Comparison of viscoelastic-type models for ocean wave attenuation in ice-covered seas. J. Geophys. Res. 120, 6072–6090.

Newyear, K., Martin, S., 1997. A comparison of theory and laboratory measurements of wave propagation and attenuation in grease ice. J. Geophys. Res. 102, 25091–25099.

Newyear, K., Martin, S., 1999. Comparison of laboratory data with a viscous two-layer model of wave propagation in grease ice. J. Geophys. Res. 104, 7837–7840.

Perrie, W., Hu, Y., 1996. Air-ice-ocean momentum exchange. Part I: Energy transfer between waves and ice floes. J. Phys. Oceanogr. 26, 1705–1720.

Rogers, W.E., Thomson, J., Shen, H.H., Doble, M.J., Wadhams, P., Cheng, S., 2016. Dissipation of wind waves by pancake and frazil ice in the autumn Beaufort Sea. J. Geophys. Res. 121, 7991–8007.

Shen, H.H., 2019. Modelling ocean waves in ice-covered seas. Appl. Ocean Res. 83, 30–36.

Squire, V.A., 2020. Ocean wave interactions with sea ice: a reappraisal. Ann. Rev. Fluid Mech. 52, 37–60.

Sutherland, G., Rabault, J., Christensen, K.H., Jensen, A., 2019. A two layer model for wave dissipation in sea ice. Appl. Ocean Res. 88, 111–118.

Thomson, J., Hošeková, L., Meylan, M.H., Kohout, A.L., Kumar, N., 2021. Spurious rollover of wave attenuation rates in sea ice caused by noise in field measurements. J. Geophys. Res. 126, e2020JC016606.

Wadhams, P., Squire, V.A., Goodman, D.J., Cowan, A.M., Moore, S.C., 1988. The attenuation rates of ocean waves in the marginal ice zone. J. Geophys. Res. 93, 6799–6818.

Wang, R., Shen, H.H., 2010a. Experimental study on surface wave propagating through a grease-pancake ice mixture. Cold Reg. Sci. Technol. 61, 90–96.

Wang, R., Shen, H.H., 2010b. Gravity waves propagating into an ice-covered ocean: A viscoelastic model. J. Geophys. Res. 115, C06024.

Williams, T.D., Bennetts, L.G., Squire, V.A., Dumont, D., Bertino, L., 2013a. Wave-ice interactions in the marginal ice zone, Part 1: Theoretical foundations. Ocean Model. 71, 81–91.

Williams, T.D., Bennetts, L.G., Squire, V.A., Dumont, D., Bertino, L., 2013b. Wave-ice interactions in the marginal ice zone, Part 2: Numerical implementation and sensitivity studies along 1d transects of the ocean surface. Ocean Model. 71, 92–101.

Williams, K.L., Francois, R.E., 1992. Sea ice elastic moduli: Determination of Biot parameters using in-field velocity measurements. J. Acoust. Soc. Am. 91, 2627–2636.

Xu, L., Guyenne, P., 2009. Numerical simulation of three-dimensional nonlinear water waves. J. Comput. Phys. 228, 8446–8466.

Zhao, X., Cheng, S., Shen, H.H., 2017. Nature of wave modes in a coupled viscoelastic layer over water. J. Eng. Mech. 143, 04017114.

Zhao, X., Shen, H.H., 2015. Wave propagation in frazil/pancake, pancake, and fragmented ice covers. Cold Reg. Sci. Technol. 113, 71–80.

Zhao, X., Shen, H.H., 2018. Three-layer viscoelastic model with eddy viscosity effect for flexural-gravity wave propagation through ice cover. Ocean Model. 131, 15–23.

Zhao, X., Shen, H.H., Cheng, S., 2015. Modeling ocean wave propagation under sea ice covers. Acta Mech. Sin. 31, 1–15.